

GIPAW Pseudopotentials of *d* Elements for Solid-State NMR

Christian Tantardini ^{1,2,*} , Alexander G. Kvashnin ³  and Davide Ceresoli ^{4,*} 

¹ Department of Chemistry, UiT The Arctic University of Norway, P.O. Box 6050 Langnes, N-9037 Tromsø, Norway

² Institute of Solid State Chemistry and Mechanochemistry SB RAS, 630128 Novosibirsk, Russia

³ Skolkovo Institute of Science and Technology, Bolshoy Boulevard 30, bld. 1, 121205 Moscow, Russia; a.kvashnin@skoltech.ru

⁴ CNR-SCITEC, c/o Dipartimento di Chimica, Università degli Studi di Milano, Via Golgi 19, 20133 Milano, Italy

* Correspondence: christiantantardini@gmail.com (C.T.); davide.ceresoli@cnr.it (D.C.)

Abstract: Computational methods are increasingly used to support interpreting, assigning and predicting the solid-state nuclear resonance magnetic spectra of materials. Currently, density functional theory is seen to achieve a good balance between efficiency and accuracy in solid-state chemistry. To be specific, density functional theory allows the assignment of signals in nuclear resonance magnetic spectra to specific sites and can help identify overlapped or missing signals from experimental nuclear resonance magnetic spectra. To avoid the difficulties correlated to all-electron calculations, a gauge including the projected augmented wave method was introduced to calculate nuclear resonance magnetic parameters with great success in organic crystals in the last decades. Thus, we developed a gauge including projected augmented pseudopotentials of 21 *d* elements and tested them on, respectively, oxides or nitrides (semiconductors), calculating chemical shift and quadrupolar coupling constant. This work can be considered the first step to improving the ab initio prediction of nuclear magnetic resonance parameters, and leaves open the possibility for inorganic compounds to constitute an alternative standard compound, with respect to tetramethylsilane, to calculate the chemical shift. Furthermore, this work represents the possibility to obtain results from first-principles calculations, to train a machine-learning model to solve or refine structures using predicted nuclear magnetic resonance spectra.

Keywords: GIPAW; *d* elements; NMR; chemical shift; quadrupolar coupling constant



Citation: Tantardini, C.; Kvashnin, A. G.; Ceresoli, D. GIPAW Pseudopotentials of *d* Elements for Solid-State NMR. *Materials* **2022**, *15*, 3347. <https://doi.org/10.3390/ma15093347>

Academic Editor: Alina Pruna

Received: 8 February 2022

Accepted: 27 April 2022

Published: 6 May 2022

Publisher's Note: MDPI stays neutral with regard to jurisdictional claims in published maps and institutional affiliations.



Copyright: © 2022 by the authors. Licensee MDPI, Basel, Switzerland. This article is an open access article distributed under the terms and conditions of the Creative Commons Attribution (CC BY) license (<https://creativecommons.org/licenses/by/4.0/>).

1. Introduction

The application of NMR spectroscopy to rigid or semi-rigid solid samples allows the study a plan of systems as bio-molecules with high molecular weight, polymers, perovskites (e.g., solar cells absorbers) and cements in chemistry and chemical sciences. NMR is the oscillatory response of nuclei with non-zero nuclear spins (total angular momentum) immersed in an external field (\mathbf{B}_0). The presence of \mathbf{B}_0 removes the degeneracy of nuclear spins, leading to the energy difference:

$$\Delta E = \gamma \hbar (1 - \sigma) \mathbf{B}_0 \quad (1)$$

where γ is the gyromagnetic ratio; and σ is the chemical shielding around a nucleus, which is a characteristic of a specific isotope. Thus, the chemical structure can be revealed by NMR frequencies that are significantly affected by γ and σ . NMR frequencies are reported as a chemical shift (δ), which is the fractional difference between the frequency of a particular nucleus and a standard compound such as tetramethylsilane (TMS). If NMR seems to be, abstractly, the best way to determine chemical structure, the NMR frequencies are strictly anisotropic, being dependent on the relative orientation between \mathbf{B}_0 and a sample, with the

consequent generation of internuclear couplings and quadrupolar couplings. Actually, the quadrupolar coupling constant (C_Q) can be estimated as

$$C_Q = \frac{eQV_{zz}}{h} \quad (2)$$

where eQ is the electric quadrupole moment, V_{zz} is the potential of electric field \mathbf{B}_0 along z -axes, and h is the Planck constant. Thus, these anisotropic interactions need to be partially averaged through the molecular rotations, and measurement of motionally averaged NMR spectra and induced nuclear spin relaxation reveals the geometries and rates of motion. Furthermore, the nuclear magnetic resonance (NMR) signal is orders of magnitude lower in frequency than the microwave, infrared and ultraviolet frequencies employed in rotational, vibrational and electronic spectroscopies. This is due to the low population difference between nuclei with removed degeneracy and those in the ground state, causing low signal-to-noise ratios along the spectra. In solid-state NMR, low signal-to-noise ratio is accentuated by the presence of acoustic phonon deformation potential (ADP) scattering and optical phonon branches. They can be responsible for electron-phonon coupling, which can, alternatively, affect the population difference. Thus, the development of NMR is focused on the increasing of experimental sensitivity. This can be carried out through increasing the intensity of an applied magnetic field, with the consequent increase in ΔE , but it is very expensive. Or it can be carried out by recording NMR spectra in the domain following a radio-frequency pulse and obtaining the spectrum by Fourier transformation rather than by sweeping the frequency and measuring absorption or emission in classical spectra. Fourier transformation NMR spectroscopy increases by one order of magnitude and opens the door to multidimensional NMR spectroscopy. In spite of its sensitivity, the interpretation of NMR spectra can be less intuitive than microscopy or diffraction data, because structural information is encoded in frequency spectra rather than spatial density maps. The frequency peaks need to be assigned to individual atoms, which can be a significant challenge. However, the multitude of peaks in NMR spectra represent an exquisite chemical fingerprint of molecules, thus making NMR spectroscopy of great use to chemists. Thus, computational methods are increasingly used to support interpreting, assigning and predicting the solid-state NMR spectra of materials. Furthermore, density functional theory (DFT) gave excellent results with gauges including atomic orbitals [1] (GIAO) for soft-matter NMR; this approach cannot be applied to solid-state NMR, because all-electron calculations are not performable due to required computational resources and the necessity to preserve translation symmetry in solids. Thus, in the framework of plane-waves DFT, a gauge including the projected augmented wave [2,3] (GIPAW) method was introduced to calculate nuclear resonance magnetic (NMR) parameters in solids, avoiding all-electron calculations. In the GIPAW approach [4,5], a uniform magnetic field is applied using boundary conditions, a *periodic magnetic field* with a finite wavelength r_G is the gauge origin and is subsequently extrapolated in the limit $r_G \rightarrow 0$ to compute the chemical shielding. This formalism was seen to manage the numerical instabilities associated with the summation of two divergent terms and with the generalized gradient approximation exchange-correlation functional (the method of choice for condensed-matter simulations) to perform accurate results [6–15]. In this work we have developed GIPAW pseudopotentials for the elements of first, second and third rows of d elements excluding La, which is considered as a part of the Lanthanides. These pseudopotentials were tested on the oxides or nitrides optimizing the crystal structures and, subsequently, we calculated the NMR parameters. The developing of these pseudopotentials was carried out to increase the number of compounds for which NMR parameters can be calculated.

2. Theoretical Background

In plane-waves DFT the all-electron potential of an atom is substituted by a mathematical object, the so-called pseudopotential. The all-electron wave functions are substituted by pseudo-wavefunctions that eliminate the core states and describe only the chosen valence

pseudo-wavefunctions. This limits the generation of a pseudopotential with a specific configuration. Actually, there are different types of pseudopotential: norm-conserving [16], ultrasoft [17] and projected augmented wave (PAW) [18]. The last introduces a linear operator

$$\Gamma = \mathbf{1} + \sum_{\mathbf{R},n} (|\phi_{\mathbf{R},n}\rangle - |\tilde{\phi}_{\mathbf{R},n}\rangle) \langle \tilde{p}_{\mathbf{R},n}| \quad (3)$$

that converts the pseudo-wavefunctions $|\tilde{\phi}_{\mathbf{R},n}\rangle$ to all-electron wavefunctions $|\phi_{\mathbf{R},n}\rangle$. In addition, $\langle \tilde{p}_{\mathbf{R},n}|$ is a set of projectors such that $\langle \tilde{p}_{\mathbf{R},n}|\tilde{\phi}_{\mathbf{R},n}\rangle = \delta_{\mathbf{R},\mathbf{R}'}\delta_{n,m}$.

Thus, it is possible to introduce in the Blochl formalism [19] a field dependent transformation operator $\Gamma_{\mathbf{B}}$ that restores the translational invariance.

$$\Gamma_{\mathbf{B}} = \mathbf{1} + \sum_{\mathbf{R},n} e^{(i/2c)\mathbf{r}\cdot\mathbf{R}\times\mathbf{B}} (|\phi_{\mathbf{R},n}\rangle - |\tilde{\phi}_{\mathbf{R},n}\rangle) \langle \tilde{p}_{\mathbf{R},n}| e^{-(i/2c)\mathbf{r}\cdot\mathbf{R}\times\mathbf{B}} \quad (4)$$

Such re-formalism is called gauge including projected augmented wave (GIPAW) [2,3] and satisfies the translation relation $|\Psi\rangle = \Gamma_{\mathbf{B}}|\tilde{\Psi}\rangle$. The GIPAW pseudo-operator $\bar{O} = \Gamma_{\mathbf{B}}^{\dagger} O \Gamma_{\mathbf{B}}$, corresponding to a local or a semilocal operator O , is given by

$$\begin{aligned} \bar{O} = & O + \sum_{\mathbf{R},n,m} e^{(i/2c)\mathbf{r}\cdot\mathbf{R}\times\mathbf{B}} |\tilde{p}_{\mathbf{R},n}\rangle \\ & \times (\langle \phi_{\mathbf{R},n}| e^{-(i/2c)\mathbf{r}\cdot\mathbf{R}\times\mathbf{B}} O e^{(i/2c)\mathbf{r}\cdot\mathbf{R}\times\mathbf{B}} |\phi_{\mathbf{R},m}\rangle \\ & - \langle \tilde{\phi}_{\mathbf{R},n}| e^{-(i/2c)\mathbf{r}\cdot\mathbf{R}\times\mathbf{B}} O e^{(i/2c)\mathbf{r}\cdot\mathbf{R}\times\mathbf{B}} |\tilde{\phi}_{\mathbf{R},m}\rangle) \\ & \times \langle \tilde{p}_{\mathbf{R},m}| e^{(i/2c)\mathbf{r}\cdot\mathbf{R}\times\mathbf{B}} \end{aligned} \quad (5)$$

The GIPAW [2,3] method allows the calculation of an induced magnetic field at the nucleus position $\mathbf{B}_{ind}(\mathbf{r})$ to the applied external magnetic field $\mathbf{B}_0(\mathbf{r})$, according to:

$$\mathbf{B}_{ind}(\mathbf{r}) = -\sigma(\mathbf{r}) \cdot \mathbf{B}_0(\mathbf{r}) \quad (6)$$

where σ is the magnetic shielding tensor that proceeds through the calculation of the first-order induced current density $\mathbf{j}^{(1)}(\mathbf{r})$, which reads:

$$\begin{aligned} \mathbf{j}^{(1)}(\mathbf{r}) = & -\sum_i^{occ} (\phi_i^0(\mathbf{r}) \nabla \phi_i^1(\mathbf{r}) + \phi_i^1(\mathbf{r}) \nabla \phi_i^0(\mathbf{r})) - \frac{1}{c} n_0 \mathbf{A}(\mathbf{r}) \\ = & \mathbf{j}_p^{(1)}(\mathbf{r}) + \mathbf{j}_d^{(1)}(\mathbf{r}) \end{aligned} \quad (7)$$

The summation runs over the occupied states and $n_0(r)$ is the unperturbed charge density. In addition, ϕ^0 are the unperturbed Kohn–Sham orbitals and their first-order counterpart, perturbed due to the external magnetic field. In Equation (7) is given the decomposition of the induced current into the so-called paramagnetic term $\mathbf{j}_p^{(1)}(\mathbf{r})$, which involves the first-order perturbed orbitals, and the diamagnetic term $\mathbf{j}_d^{(1)}(\mathbf{r})$, which depends on the unperturbed charge density. $\mathbf{A}(\mathbf{r})$ is the vector potential connected to \mathbf{B}_0 through

$$\mathbf{A}(\mathbf{r}) = \frac{1}{2} \mathbf{B}_0(\mathbf{r}) \times (\mathbf{r} - \mathbf{r}_G) \quad (8)$$

where \mathbf{r}_G is the so-called gauge origin. $\mathbf{B}_{ind}(\mathbf{r})$ is finally obtained from the Biot–Savart law:

$$\mathbf{B}_{ind}(\mathbf{r}) = \frac{1}{c} \int d\mathbf{r}_G \mathbf{j}^{(1)}(\mathbf{r}_G) \times \frac{\mathbf{r} - \mathbf{r}_G}{|\mathbf{r} - \mathbf{r}_G|^3} \quad (9)$$

Actually, there are connections between our GIPAW [2,3] approach and the GIAO [1] method widely used in the quantum-chemical community for the all-electron calculation

NMR of molecules. However, it should be recognized that, in *GIPAW* [2,3], the phase required to maintain the translational invariance is carried by the operators, whereas in the GIAO [1] approach, the field-dependent phase is attached to the basis functions and to the occupied electronic orbitals, respectively.

3. Method and Computational Details

GIPAW pseudopotentials were developed for 21 *d* elements excluding La which is considered as a part of Lanthanides, using Quantum Espresso version 6.6 [20,21] and they are written in the universal pseudopotential format (UPF) version 2 (pseudopotentials will be available to everybody as UPF2 format, see available dataset). *GIPAW* were developed solving the scalar relativistic wave equation (Koelling–Harmon-like equation) [22] with Rappe–Rabe–Efthimios–Kaxiras–Joannopoulos [23] (RRKJ) form of pseudo-wavefunctions modeled by double projectors and semi-core states. A non-linear core correction (NLCC) [24] was employed for all developed *GIPAW*s. The NLCC allows to avoid the necessity to separate spin-up and spin-down ionic pseudopotentials, treating explicitly the nonlinear exchange and correlation interaction between the core and the valence charge densities. In particular, the spin-polarized configurations are well-described with a single potential. The analysis of logarithmic derivatives, i.e., derivatives of an *l*-state $\frac{d(\log(\Psi_l(E)))}{dE}$ computed for the exact atomic problem and with the *GIPAW* dataset, was computed to verify the presence of highly-localized negative energy ghosts that could affect the quality of pseudopotential. No element presented highly localized negative-energy ghosts and only highly localized positive-energy ghosts are seen in the *d* orbital of Nb Os and Ta, but they are located too high in energy (i.e., 1 Ry for Nb and Os, 4 Ry for Ta) to affect the quality of pseudopotential also, cases with the promotion of one electron in the *d* orbital will be described. All the logarithmic derivatives and NLCC for each pseudopotential are shown in the available data. Considered oxides and nitrides of *d* elements of first-, second- and third-period, which are semiconductors, were fully optimized in Quantum Espresso version 6.6 [20,21] with previously developed *GIPAW* [2,3] of *d* elements for PBE exchange-correlation density functional [25]. The crystal structures were taken from Material Project [26] and are here identified by their mp-code: AgN₃, mp-571297; Au₂O₃, mp-27253; CdO₂, mp-2310; Cr₂O₃, mp-19399; HgO, mp-1224; IrN₂, mp-415; Lu₂O₃, mp-1427; MoO₃, mp-18856; Nb₂O₅, mp-581967; OsO₄, mp-540783; PdN₂, mp-1103427; PtO₂, mp-7868; Re₂O₇, mp-1016092; Rh₂O₃, mp-542734; RuO₄, mp-554791; Sc₂O₃, mp-216; Ta₂O₅, mp-10390; Tc₂O₇, mp-27485; V₂O₅, mp-25279; WO₃, mp-18773; Y₂O₃, mp-2652. All above-mentioned structures are fully optimized with PBE exchange-correlation density functional [25]. The geometry optimization relies on Broyden–Fletcher–Goldfarb–Shanno (BFGS) algorithm [27–30], with force tolerance for the maximum net force on atoms fixed at 10^{−6} Ry/Angstrom and the total energy at 10^{−8} Ry. The kinetic energy plane-wave energy cutoff of 100 Ry, and the Gaussian smearing [31] equal to 0.005 eV were chosen for all structures. The Γ -centered k-point meshes are: 3 × 3 × 3 for AgN₃, and CdO₂; 4 × 2 × 2 for Au₂O₃, Cr₂O₃, and Re₂O₇; 3 × 6 × 6 for HgO; 6 × 6 × 6 for IrN₂; 4 × 4 × 4 for Lu₂O₃, MoO₃, PdN₂, RuO₄, and WO₃; 2 × 4 × 4 for Nb₂O₅, OsO₄, and Ta₂O₅; 6 × 6 × 3 for PtO₂; 4 × 4 × 2 for Rh₂O₃, and V₂O₅; 2 × 2 × 2 for Sc₂O₃, and Y₂O₃; and 6 × 4 × 2 for Tc₂O₇. The computation of NMR shielding tensors was performed with the *GIPAW* module for Quantum Espresso version 6.6 [20,21].

4. Results and Discussion

In metal transitions, the so-called semi-core states overlap with the *d*-valence states. Thus, we introduced the semi-core states in valence states with a small core region radius, improving the accuracy. For the 3*d* transition metals, the semi-states 3*s* 3*p* 3*d* were chosen as part of the valence partition. The *GIPAW*s for the 4*d* transition metals all contain the 4*s* 4*p* 4*d* semi-states in the valence. For the 5*d* transition metals, the 5*s* 5*p* 5*d* semi-states are contained in the valence of *GIPAW*s. In 5*d* transition metals, 4*f* states were frozen due to the complexity, to be rightly described lying at the same energy range as the 5*s* and 5*p* states. It is noteworthy that, for such elements, the ground-state properties can be described well enough with 4*f* frozen. Meanwhile,

for optical properties and *GW* approximation [32,33], this may not be the case. This is the case even for elements such as Au, where the *4f* electrons lie about 3 Ha below the Fermi level. Instead, for *GIPAW* for *3d* and *4d* elements, *GW* approximation [32,33] can also be performed with such pseudopotentials. The ground-state properties of *5d* elements are not affected by *4f* orbitals because they are contracted close to the core due to relativistic effects and consequent *jj*-spin orbit coupling. This means that, firstly, for each orbital its orbital angular momentum is coupled with the magnetic angular momentum of the electron located in such an orbital, obtaining an angular momentum *j* and, subsequently, all these *j* are coupled to make the total angular momentum of a heavy atom. We fully relaxed the crystal structures of the oxides and nitrides of the 21 *d* elements of which we developed *GIPAW* pseudopotentials using the PBE DFT functional. The PBE DFT functional is known in the literature to overestimate the unit volume by close to 4–4.5%, but the agreement between the calculated and experimental NMR parameters is generally found to be significantly improved after the DFT optimization of the structure geometry [34]. This motivated our choice to optimize the structure before calculating the NMR parameters. We are aware that all oxides and nitrides of *d* elements are considered strong correlated systems. This means that heuristic DFT alone seems to not be enough to describe correctly the electronic structure spreading the *d* electrons within the unit cell. Usually, DFT+U [35] typically works well for strongly correlated systems localizing the *d* electrons on metals, but previous works showed that the *GIPAW* formalism feasibly describes the transition metals with an heuristic DFT [36–39]. Thus, we have used a heuristic DFT to fully relax the chosen systems. The fully optimized lattice parameters of such systems agree with those that come from experiments and with the computed structures showed in Material Project [26], see Figure 1 and Tables S1 and S2 in Supporting Information. Such computed structures, reported in Material Project [26], were actually optimized using projector augmented-wave (PAW) pseudopotentials [19] in VASP code [40–43]. Confident of the quality of the obtained lattice parameters of the oxides and nitrides of the *d* elements, we were able to use the *GIPAW* approach to calculate the total NMR chemical shift (σ) by adopting the Simpson [44] convention for anisotropy and asymmetry and the average value of the *d* elements within the oxide or nitrides are reported in Table 1. We have reported, in Table 1, the average values because, in some structures, the atoms that are in non-equivalent for symmetry positions have different values and in Supporting Information from Tables S3–S23 we reported all atomic positions with corresponding (σ). It is noteworthy that we have obtained negative (σ) in some cases and this is due to the fact that some *d* elements are more shielded with respect to the chosen reference (i.e., TMS) compound. This make us to consider if the evolution of NMR should be focused to find an inorganic compound to set σ . Indeed, here we considered nitrides or oxides that are semiconductors. Thus, our results are not affected by Knight shift, as in metals, due to the high population of *d* electrons at the Fermi level. We also calculated C_Q and its average values for the *d* elements within oxides or nitrides, see Table 1, while the value for each atom is reported in Supporting Information. Of note is the impossibility of using predicted NMR spectra from first-principles calculations to solve or refine structures due to the time and cost of the calculation, which poses challenges to a real-time automated solution. To address this problem, machine-learning approaches were introduced to calculate chemical shifts in molecular solids, which reduces computational cost by orders of magnitude while maintaining the accuracy of DFT [45]. All these machine-learning models are trained on first-principles calculations, making the latter of fundamental importance to improve the accuracy of machine-learning models.

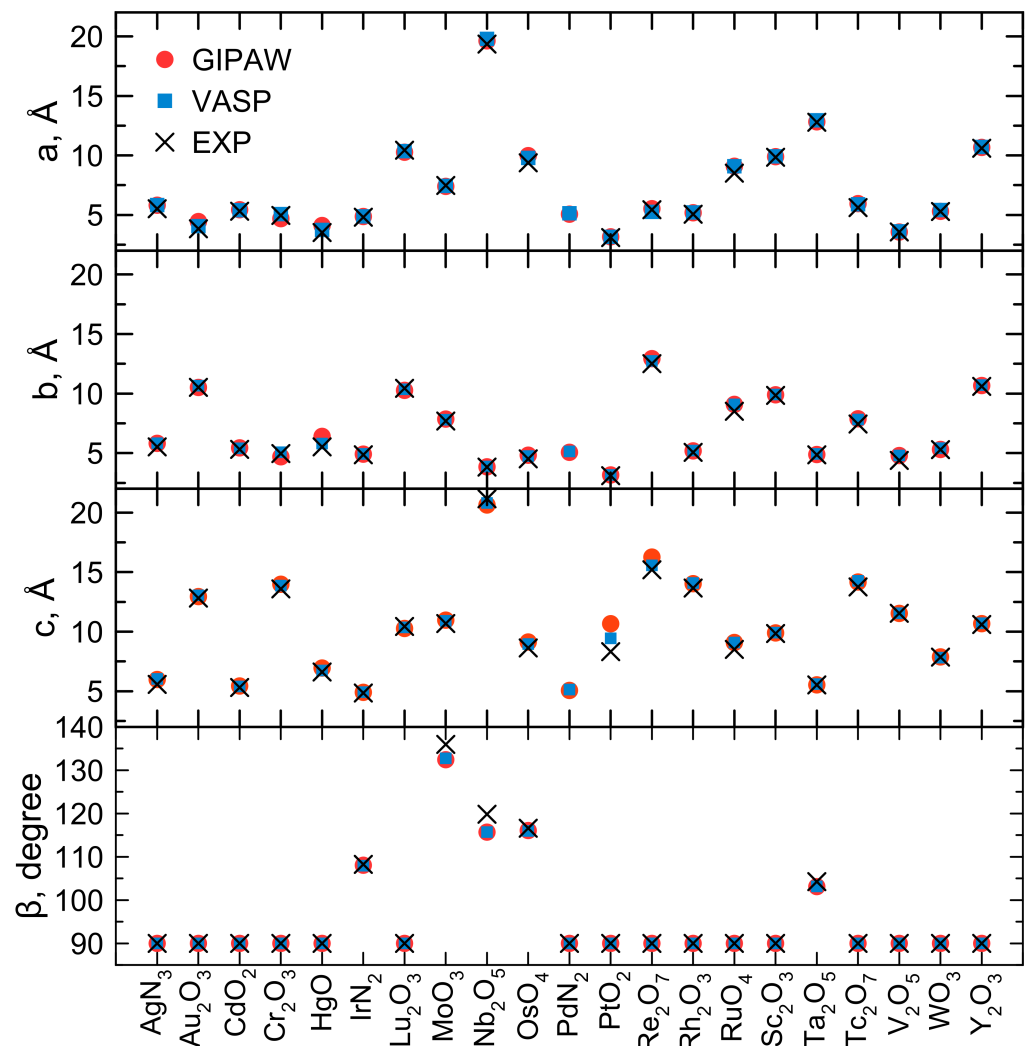


Figure 1. Lattice parameters of 21 fully relaxed unit cells with developed *GIPAW* pseudopotentials (red circles) compared with those optimized with PAW pseudopotentials in VASP code (cyan squares) and experimental ones (black crosses).

Table 1. Average of total chemical shift $\bar{\sigma}$ in ppm and the average of quadrupolar coupling constant \bar{C}_Q in MHz for each *d* element within their oxides or nitrides.

System	$\bar{\sigma}$	\bar{C}_Q	System	$\bar{\sigma}$	\bar{C}_Q
AgN ₃	2542.54	0.04	PtO ₂	−7557.22	1.20
Au ₂ O ₃	1115.14	2.45	Re ₂ O ₇	−1064.07	3.44
CdO ₂	3322.38	0.09	Rh ₂ O ₃	−10,829.68	0.05
Cr ₂ O ₃	−6933.31	−0.07	RuO ₄	−2968.18	0.02
HgO	6700.46	−15.05	Sc ₂ O ₃	677.59	−0.25
IrN ₂	−4132.37	−4.95	Ta ₂ O ₅	2529.32	2.76
Lu ₂ O ₃	5317.24	−1.03	Tc ₂ O ₇	−2249.87	0.43
MoO ₃	−1196.63	−2.30	V ₂ O ₅	−1447.62	−0.35
Nb ₂ O ₅	102.85	−1.06	WO ₃	752.99	5.18
OsO ₄	−2337.18	−0.06	Y ₂ O ₃	1928.05	−0.41
PdN ₂	−3407.89	−0.37			

5. Conclusions

In this work, we developed *GIPAW* pseudopotentials for 21 *d* elements and tested them on their oxides or nitrides. The developed pseudopotentials present semi-core states to increase their flexibility, to be employed in several compounds with feasible approximation, and are free of ghosts states, making them conceptually right. The obtained σ and C_Q for the *d* elements seem to be coherent with expected values for such elements, respectively, in their oxides or nitrides. The *GIPAW* pseudopotentials increase the number of compounds for which it will be possible to calculate the NMR parameters with first-principle calculations and subsequently use them to develop machine learning models for real-time refining structure from NMR spectra.

Supplementary Materials: The following supporting information can be downloaded at: <https://www.mdpi.com/article/10.3390/ma15093347/s1>, Table S1: Table of lattice parameters of 10 fully-relaxed unit cells with developed *GIPAW* pseudopotentials and those optimized with PAW pseudopotentials in VASP code and the experimental ones; Table S2: Table of lattice parameters of 11 fully-relaxed unit cells with developed *GIPAW* pseudopotentials and those optimized with PAW pseudopotentials in VASP code and the experimental ones; Table S3: Atomic crystallographic positions with vectors lattice in Angstrom of AgN_3 with total chemical shift σ in ppm and quadrupolar coupling constant C_Q in MHz for each element; Table S4: Atomic crystallographic positions with vectors lattice in Angstrom of Au_2O_3 with total chemical shift σ in ppm and quadrupolar coupling constant C_Q in MHz for each element; Table S5: Atomic crystallographic positions with vectors lattice in Angstrom of CdO_2 with total chemical shift σ in ppm and quadrupolar coupling constant C_Q in MHz for each element; Table S6: Atomic crystallographic positions with vectors lattice in Angstrom of Cr_2O_3 with total chemical shift σ in ppm and quadrupolar coupling constant C_Q in MHz for each element; Table S7: Atomic crystallographic positions with vectors lattice in Angstrom of HgO with total chemical shift σ in ppm and quadrupolar coupling constant C_Q in MHz for each element; Table S8: Atomic crystallographic positions with vectors lattice in Angstrom of IrN_2 with total chemical shift σ in ppm and quadrupolar coupling constant C_Q in MHz for each element; Table S9: Atomic crystallographic positions with vectors lattice in Angstrom of Lu_2O_3 with total chemical shift σ in ppm and quadrupolar coupling constant C_Q in MHz for each element; Table S10: Atomic crystallographic positions with vectors lattice in Angstrom of MoO_3 with total chemical shift σ in ppm and quadrupolar coupling constant C_Q in MHz for each element; Table S11: Atomic crystallographic positions with vectors lattice in Angstrom of Nb_2O_5 with total chemical shift σ in ppm and quadrupolar coupling constant C_Q in MHz for each element; Table S12: Atomic crystallographic positions with vectors lattice in Angstrom of OsO_4 with total chemical shift σ in ppm and quadrupolar coupling constant C_Q in MHz for each element; Table S13: Atomic crystallographic positions with vectors lattice in Angstrom of PdN_2 with total chemical shift σ in ppm and quadrupolar coupling constant C_Q in MHz for each element; Table S14: Atomic crystallographic positions with vectors lattice in Angstrom of PtO_2 with total chemical shift σ in ppm and quadrupolar coupling constant C_Q in MHz for each element; Table S15: Atomic crystallographic positions with vectors lattice in Angstrom of Re_2O_7 with total chemical shift σ in ppm and quadrupolar coupling constant C_Q in MHz for each element; Table S16: Atomic crystallographic positions with vectors lattice in Angstrom of Rh_2O_3 with total chemical shift σ in ppm and quadrupolar coupling constant C_Q in MHz for each element; Table S17: Atomic crystallographic positions with vectors lattice in Angstrom of RuO_4 with total chemical shift σ in ppm and quadrupolar coupling constant C_Q in MHz for each element; Table S18: Atomic crystallographic positions with vectors lattice in Angstrom of Sc_2O_3 with total chemical shift σ in ppm and quadrupolar coupling constant C_Q in MHz for each element; Table S19: Atomic crystallographic positions with vectors lattice in Angstrom of Ta_2O_5 with total chemical shift σ in ppm and quadrupolar coupling constant C_Q in MHz for each element; Table S20: Atomic crystallographic positions with vectors lattice in Angstrom of Tc_2O_7 with total chemical shift σ in ppm and quadrupolar coupling constant C_Q in MHz for each element; Table S21: Atomic crystallographic positions with vectors lattice in Angstrom of V_2O_5 with total chemical shift σ in ppm and quadrupolar coupling constant C_Q in MHz for each element; Table S22: Atomic crystallographic positions with vectors lattice in Angstrom of WO_3 with total chemical shift σ in ppm and quadrupolar coupling constant C_Q in MHz for each element; Table S23: Atomic crystallographic positions with

vectors lattice in Angstrom of Y_2O_3 with total chemical shift σ in ppm and quadrupolar coupling constant C_Q in MHz for each element.

Author Contributions: Conceptualization, C.T. and D.C.; methodology, C.T. and D.C.; software, C.T. and D.C.; validation, C.T. and D.C.; formal analysis, C.T., A.G.K. and D.C.; investigation, C.T. and D.C.; resources, C.T.; data curation, C.T., A.G.K. and D.C.; writing—original draft preparation, C.T. and A.G.K.; writing—review and editing, C.T., A.G.K. and D.C.; visualization, C.T., A.G.K. and D.C.; supervision, C.T. and D.C.; project administration, C.T. and D.C.; funding acquisition, C.T. and D.C. All authors have read and agreed to the published version of the manuscript.

Funding: This work was supported by Russian state assignment to ISSCM SB RAS (project No. FWUS-2021-0005).

Institutional Review Board Statement: Not applicable.

Informed Consent Statement: Not applicable.

Data Availability Statement: Dataset folder with all generated UPF2 format pseudopotentials will be accessible to the link <https://sites.google.com/site/dceresoli/pseudopotentials> (accessed on 7 February 2022).

Acknowledgments: The authors would like to thank the Siberian Super-Computer Center of the Siberian Branch of the Russian Academy of Sciences and Sigma2-the National Infrastructure for High Performance Computing Data Storage in Norway-for computational resources. The authors would like to thank X. Gonze and M. Giantomassi of UCLouvain and P. Giannozzi of University of Udine for useful discussion.

Conflicts of Interest: The authors declare no conflict of interest.

References

1. Ditchfield, R. Molecular Orbital Theory of Magnetic Shielding and Magnetic Susceptibility. *J. Chem. Phys.* **1972**, *56*, 5688–5691. [[CrossRef](#)]
2. Pickard, C.J.; Mauri, F. All-electron magnetic response with pseudopotentials: NMR chemical shifts. *Phys. Rev. B* **2001**, *63*, 245101. [[CrossRef](#)]
3. Joyce, S.A.; Yates, J.R.; Pickard, C.J.; Mauri, F. A first principles theory of nuclear magnetic resonance J-coupling in solid-state systems. *J. Chem. Phys.* **2007**, *127*, 204107. [[CrossRef](#)] [[PubMed](#)]
4. Charpentier, T. The PAW/GIPAW approach for computing NMR parameters: A new dimension added to NMR study of solids. *Solid State Nucl. Magn. Reson.* **2011**, *40*, 1–20. [[CrossRef](#)] [[PubMed](#)]
5. Ferreira, A.R. DFT-GIPAW 27Al NMR Simulations for Intermetallics: Accuracy Issues and Magnetic Screening Mechanisms. *J. Phys. Chem. C* **2019**, *123*, 9371–9381. [[CrossRef](#)]
6. Moudrakovski, I.; Lang, S.; Patchkovskii, S.; Ripmeester, J. High Field ^{33}S Solid State NMR and First-Principles Calculations in Potassium Sulfates. *J. Phys. Chem. A* **2010**, *114*, 309–316. [[CrossRef](#)] [[PubMed](#)]
7. Johansson, E.M.J.; Yartsev, A.; Rensmo, H.; Sundström, V. Photocurrent Spectra and Fast Kinetic Studies of P3HT/PCBM Mixed with a Dye for Photoconversion in the Near-IR Region. *J. Phys. Chem. C* **2009**, *113*, 3014–3020. [[CrossRef](#)]
8. Widdifield, C.M.; Bryce, D.L. Solid-State $^{79/81}Br$ NMR and Gauge-Including Projector-Augmented Wave Study of Structure, Symmetry, and Hydration State in Alkaline Earth Metal Bromides. *J. Phys. Chem. A* **2010**, *114*, 2102–2116. [[CrossRef](#)]
9. Lister, S.E.; Soleilhavoup, A.; Withers, R.L.; Hodgkinson, P.; Evans, J.S.O. Structures and Phase Transitions in $(MoO_2)_2P_2O_7$. *Inorg. Chem.* **2010**, *49*, 2290–2301. [[CrossRef](#)]
10. Sutrisno, A.; Terskikh, V.V.; Huang, Y. A natural abundance ^{33}S solid-state NMR study of layered transition metaldisulfides at ultrahigh magnetic field. *Chem. Commun.* **2009**, *2*, 186–188. [[CrossRef](#)]
11. Griffin, J.M.; Wimperis, S.; Berry, A.J.; Pickard, C.J.; Ashbrook, S.E. Solid-State ^{17}O NMR Spectroscopy of Hydrous Magnesium Silicates: Evidence for Proton Dynamics. *J. Phys. Chem. C* **2009**, *113*, 465–471. [[CrossRef](#)]
12. Choi, M.; Matsunaga, K.; Oba, F.; Tanaka, I. ^{27}Al NMR Chemical Shifts in Oxide Crystals: A First-Principles Study. *J. Phys. Chem. C* **2009**, *113*, 3869–3873. [[CrossRef](#)]
13. Dumez, J.N.; Pickard, C.J. Calculation of NMR chemical shifts in organic solids: Accounting for motional effects. *J. Chem. Phys.* **2009**, *130*, 104701. [[CrossRef](#)] [[PubMed](#)]
14. Hung, I.; Uldry, A.C.; Becker-Baldus, J.; Webber, A.L.; Wong, A.; Smith, M.E.; Joyce, S.A.; Yates, J.R.; Pickard, C.J.; Dupree, R.; et al. Probing Heteronuclear ^{15}N - ^{17}O and ^{13}C - ^{17}O Connectivities and Proximities by Solid-State NMR Spectroscopy. *J. Am. Chem. Soc.* **2009**, *131*, 1820–1834. [[CrossRef](#)]
15. O'Dell, L.A.; Schurko, R.W. Static solid-state ^{14}N NMR and computational studies of nitrogen EFG tensors in some crystalline amino acids. *Phys. Chem. Chem. Phys.* **2009**, *11*, 7069–7077. [[CrossRef](#)] [[PubMed](#)]

16. Bachelet, G.B.; Hamann, D.R.; Schlüter, M. Pseudopotentials that work: From H to Pu. *Phys. Rev. B* **1982**, *26*, 4199–4228. [[CrossRef](#)]
17. Vanderbilt, D. Soft self-consistent pseudopotentials in a generalized eigenvalue formalism. *Phys. Rev. B* **1990**, *41*, 7892–7895. [[CrossRef](#)] [[PubMed](#)]
18. Blöchl, P.E. Projector augmented-wave method. *Phys. Rev. B* **1994**, *50*, 17953–17979. [[CrossRef](#)]
19. Kresse, G.; Joubert, D. From ultrasoft pseudopotentials to the projector augmented-wave method. *Phys. Rev. B* **1999**, *59*, 1758–1775. [[CrossRef](#)]
20. Giannozzi, P.; Baroni, S.; Bonini, N.; Calandra, M.; Car, R.; Cavazzoni, C.; Ceresoli, D.; Chiarotti, G.L.; Cococcioni, M.; Dabo, I.; et al. QUANTUM ESPRESSO: A modular and open-source software project for quantum simulations of materials. *J. Phys. Condens. Matter* **2009**, *21*, 395502. [[CrossRef](#)]
21. Giannozzi, P.; Baseggio, O.; Bonfà, P.; Brunato, D.; Car, R.; Carnimeo, I.; Cavazzoni, C.; de Gironcoli, S.; Delugas, P.; Ferrari Ruffino, F.; et al. Quantum ESPRESSO toward the exascale. *J. Chem. Phys.* **2020**, *152*, 154105. [[CrossRef](#)]
22. Koelling, D.D.; Harmon, B.N. A technique for relativistic spin-polarised calculations. *J. Phys. Solid State Phys.* **1977**, *10*, 3107–3114. [[CrossRef](#)]
23. Rappe, A.M.; Rabe, K.M.; Kaxiras, E.; Joannopoulos, J.D. Optimized pseudopotentials. *Phys. Rev. B* **1990**, *41*, 1227–1230. [[CrossRef](#)]
24. Louie, S.G.; Froyen, S.; Cohen, M.L. Nonlinear ionic pseudopotentials in spin-density-functional calculations. *Phys. Rev. B* **1982**, *26*, 1738–1742. [[CrossRef](#)]
25. Perdew, J.P.; Ernzerhof, M.; Burke, K. Rationale for mixing exact exchange with density functional approximations. *J. Chem. Phys.* **1996**, *105*, 9982. [[CrossRef](#)]
26. Jain, A.; Ong, S.P.; Hautier, G.; Chen, W.; Richards, W.D.; Dacek, S.; Cholia, S.; Gunter, D.; Skinner, D.; Ceder, G.; et al. The Materials Project: A materials genome approach to accelerating materials innovation. *APL Mater.* **2013**, *1*, 011002. [[CrossRef](#)]
27. Brody, C.G. The Convergence of a Class of Double-Rank Minimization Algorithms 1. General Considerations. *IMA J. Appl. Math.* **1970**, *6*, 76–90. [[CrossRef](#)]
28. Goldfarb, D. A Family of Variable-Metric Methods Derived by Variational Means. *Math. Comp.* **1970**, *24*, 23–26. [[CrossRef](#)]
29. Shanno, D.F. Conditioning of Quasi-Newton Methods for Function Minimization. *Math. Comp.* **1970**, *24*, 647–656. [[CrossRef](#)]
30. Steihaug, T. *Practical Methods of Optimization Volume 1: Unconstrained Optimization*; Wiley: New York, NY, USA, 1980.
31. Ho, K.M.; Fu, C.L.; Harmon, B.N.; Weber, W.; Hamann, D.R. Vibrational Frequencies and Structural Properties of Transition Metals via Total-Energy Calculations. *Phys. Rev. Lett.* **1982**, *49*, 673–676. [[CrossRef](#)]
32. Hedin, L. New Method for Calculating the One-Particle Green's Function with Application to the Electron-Gas Problem. *Phys. Rev. A* **1965**, *139*, 795. [[CrossRef](#)]
33. Martin, R.M.; Reining, L.; Ceperley, D. *Interacting Electrons*; Cambridge University Press: Cambridge, UK, 2016.
34. Yates, J.R.; Dobbins, S.E.; Pickard, C.J.; Mauri, F.; Ghi, P.Y.; Harris, R.K. A combined first principles computational and solid-state NMR study of a molecular crystal: flurbiprofen. *Phys. Chem. Chem. Phys.* **2005**, *7*, 1402–1407. [[CrossRef](#)]
35. Cococcioni, M.; de Gironcoli, S. Linear response approach to the calculation of the effective interaction parameters in the LDA + U method. *Phys. Rev. B* **2005**, *71*, 035105. [[CrossRef](#)]
36. Trinité, V.; Vast, N.; Hayoun, M. Effects of localization of the semicore density on the physical properties of transition and noble metals. *J. Phys. Condens. Matter* **2008**, *20*, 235239. [[CrossRef](#)]
37. Cramer, C.J.; Truhlar, D.G. Density functional theory for transition metals and transition metal chemistry. *Phys. Chem. Chem. Phys.* **2009**, *11*, 10757–10816. [[CrossRef](#)]
38. Hansen, M.R.; Madsen, G.K.H.; Jakobsen, H.J.; Skibsted, J. Evaluation of ^{27}Al and ^{51}V Electric Field Gradients and the Crystal Structure for Aluminum Orthovanadate (AlVO_4) by Density Functional Theory Calculations. *J. Phys. Chem. B* **2006**, *110*, 5975–5983. [[CrossRef](#)]
39. Yan, Z.; Chen, B.; Huang, Y. A solid-state NMR study of the formation of molecular sieve SAPO-34. *Solid State Nucl. Magn. Reson.* **2009**, *35*, 49–60. [[CrossRef](#)] [[PubMed](#)]
40. Kresse, G.; Hafner, J. Ab initio molecular dynamics for liquid metals. *Phys. Rev. B* **1993**, *47*, 558–561. [[CrossRef](#)]
41. Kresse, G.; Hafner, J. Ab initio molecular dynamics for open-shell transition metals. *Phys. Rev. B* **1993**, *48*, 13115–13118. [[CrossRef](#)]
42. Kresse, G.; Furthmüller, J.; Hafner, J. Theory of the crystal structures of selenium and tellurium: The effect of generalized-gradient corrections to the local-density approximation. *Phys. Rev. B* **1994**, *50*, 13181–13185. [[CrossRef](#)]
43. Kresse, G.; Furthmüller, J.; Hafner, J. Ab initio Force Constant Approach to Phonon Dispersion Relations of Diamond and Graphite. *Europhys. Lett. (EPL)* **1995**, *32*, 729–734. [[CrossRef](#)]
44. Bak, M.; Rasmussen, J.T.; Nielsen, N.C. SIMPSON: A General Simulation Program for Solid-State NMR Spectroscopy. *J. Magn. Reson.* **2000**, *147*, 296–330. [[CrossRef](#)] [[PubMed](#)]
45. Paruzzo, F.M.; Hofstetter, A.; Musil, F.; De, S.; Ceriotti, M.; Emsley, L. Chemical shifts in molecular solids by machine learning. *Nat. Commun.* **2018**, *9*, 4501. [[CrossRef](#)] [[PubMed](#)]